Nonlinear Nonmodal Analysis of Hypersonic Flow over Blunt Cones

Anton Scholten, *
North Carolina State University, Raleigh, NC 27695, USA

Pedro Paredes, †
National Institute of Aerospace, Hampton, VA 23666, USA

Meelan M. Choudhari, ‡ Fei Li, § Mark Carpenter, ¶
NASA Langley Research Center, Hampton, VA 23681, USA

Michelle Bailey ‖
The University of Arizona, Tucson, AZ 85721, USA

The linear amplification of modal disturbances that lead to boundary-layer transition in two-dimensional/axisymmetric hypersonic configurations is strongly reduced by the presence of a blunt nosetip, and the mechanisms underlying the observed onset of transition over the cone frustum are currently unknown. Linear nonmodal analysis has shown that both planar and oblique traveling disturbances that peak within the entropy layer experience appreciable energy amplification for moderate to large nosetip bluntness. The present study extends the previous linear analysis by including the nonlinear effects. Specifically, the perturbation form of the 2D, harmonic Navier-Stokes equations (HNSE) are solved with a fully implicit formulation and the Newton-Raphson method. The increased number of degrees of freedom for the nonlinear system presents difficulties for solution strategies based on direct solution of the linearized system. Such difficulties are overcome by using the GMRES iterative method with a preconditioner corresponding to a simplified Jacobian without the cross derivative terms. The HNSE solver is verified by comparing with nonlinear parabolized stability equation (NPSE) results for the nonlinear evolution of planar waves in an incompressible Blasius boundary layer and in a Mach 6 flow over a blunt cone. Finally, nonlinear nonmodal results are presented for planar traveling disturbances over the blunt cone. The nonmodal analysis demonstrates that entropy-layer disturbances generated close to the nose tip can seed the amplification of higher frequency Mack's second-mode instabilities further downstream.

Nomenclature

A	=	disturbance amplitude
E	=	disturbance energy
G	=	gain
h_t	=	total enthalpy [kg m^2 s^{-2}]
h_ξ	=	streamwise metric factor
h_ζ	=	azimuthal metric factor
m	=	azimuthal wavenumber [rad^{-1}]
M	=	Mach number
n	=	Fourier mode

*Graduate Student, Department of Mechanical and Aerospace Engineering. AIAA Student Member
†Senior Research Engineer, Computational AeroSciences Branch, NASA LaRC. AIAA Senior Member
‡Senior Research Scientist, Computational AeroSciences Branch. AIAA Fellow
§Senior Research Scientist, Computational AeroSciences Branch.
¶Senior Research Scientist, Computational AeroSciences Branch.
‖Graduate Student, Department of Aerospace and Mechanical Engineering, AIAA Student Member.

n_ω	=	number of Fourier modes
N	=	logarithmic amplification factor
$\hat{\mathbf{q}}$	=	vector of amplitude variables
$\check{\mathbf{q}}$	=	vector of disturbance function variables
$\bar{\mathbf{q}}$	=	vector of base flow variables
$\tilde{\mathbf{q}}$	=	vector of perturbation variables
Re_x	=	Reynolds number based on streamwise location
R	=	local Reynolds number
Re_∞	=	freestream unit Reynolds number [m^{-1}]
Re_{R_N}	=	Reynolds number based on nosetip radius
R_N	=	nosetip radius [m]
T	=	temperature [K]
T_w	=	wall temperature [K]
(u, v, w)	=	streamwise, wall-normal, and azimuthal velocity components [m s^{-1}]
(x, y, z)	=	Cartesian coordinates
α	=	streamwise wavenumber [m^{-1}]
δ_h	=	boundary-layer thickness [m]
κ	=	streamwise curvature [m^{-1}]
ω	=	disturbance angular frequency [s^{-1}]
ρ	=	density [kg m^{-3}]
(ξ, η, ζ)	=	streamwise, wall-normal, and azimuthal coordinates
Superscripts		
$*$	=	dimensional value
Subscript		
∞	=	freestream value
rms	=	root-mean-square
0	=	initial position
1	=	final position
T	=	transition location

I. Introduction

The importance of transition prediction in the hypersonic regime is paramount to the survival of a vehicle as the surface heating has a significant impact on the structure. It remains a complex issue to accurately predict the location and intensity of the transition, and canonical geometries such as flat plates and cones are used in both wind tunnel experiments and computational analyses to further understand the onset and development of transition [1–3]. A thorough review concerning boundary-layer transition on sharp and blunt cones at hypersonic speeds is provided by Schneider [4]. The review notes modal growth of Mack-mode instabilities (second-mode waves) being responsible for laminar-turbulent transition on sharp axisymmetric cones at zero degrees angle of attack. This conclusion was reached following both experimental and numerical studies. Previous work by Stetson [5] identified the effect of increasing the nosetip Reynolds number (Re_{R_N}), leading to the formation of an entropy layer stabilizing the Mack-mode instabilities, consistent with experimental results demonstrating a displacement of the transition onset downstream. But this trend eventually reverses beyond a critical nosetip bluntness. This reversal phenomenon has been explored by Paredes et al. [6], where wind tunnel measurements from Mach 6 to 10 highlighted the nosetip roughness influence on the beginning of transition.

Transition reversal has also been experimentally reported on blunted flat plates by Lysenko [7]. The transition mechanism is somewhat different from blunted cones due to shorter entropy-layer swallowing length and azimuthal spreading. Work by Goparaju et al. [8] studied the effects of leading-edge bluntness on the receptivity and stability of the boundary layer over a flat plate at zero degrees angle of attack and Mach 6 flow conditions. Direct numerical simulations (DNS) were conducted with random forcing upstream of the model. The results show a change in the induced boundary-layer disturbances as the flat-plate bluntness was increased. The instability waves for the blunter models were observed near the generalized inflection point of the entropy layer above the boundary-layer edge and resembled the nonmodal entropy-layer waves captured by Paredes et al. [9] for blunt cones. In a follow-up work, Scholten et al. [10] performed linear modal and nonmodal analysis on the same flat plate geometries at Mach 4 and 6 and obtained good agreement between the identified frequencies and spanwise wavenumbers of the most amplified

disturbances. The increase in leading edge radius of the flat plate led to a decrease in the amplification of modal instability. However, the nonmodal analysis established the appreciable amplification of disturbances in the boundary- and entropy-layer disturbances at large enough nose radius.

Experimental measurements by Hill [11] and Hill et al. [12] at the Air Force Research Laboratory Mach 6 Ludwieg Tube have focused on disturbance evolution over a series of sharp and blunt ogive-cylinder geometries. Interchangeable forebodies followed by a cylindrical section allowed instability measurements past the entropy-layer swallowing location. The ogive forebodies were designed specifically to control the shock curvature, which in turn alters the entropy layer structure and strength, both playing a crucial role in external instability growth [13, 14]. The frequency and azimuthal wavenumber of the observed disturbances were then obtained numerically by Scholten et al. [15] by using linear modal and nonmodal analyses. The disturbance shape was also compared with experimental schlieren images and validated the wall-normal location of the disturbances. The numerical study by Hartman et al. [16] targeted an oblique breakdown via a stronger nonlinear mechanism that leads to transition over a shorter downstream distance as compared to the breakdown via a fundamental or subharmonic resonance.

DNS are now offering new insights into boundary-layer transition in conventional ground facilities that suffer from acoustic noise emanating from the turbulent boundary layer over the nozzle walls and is not encountered in hypersonic flight [17–20]. The results from a hypersonic wind-tunnel DNS by Liu et al. [21] with a blunt cone of 5.2 mm at zero AoA and flow conditions of the Sandia Hypersonic Wind Tunnel 8 (HWT-8), i.e., Mach 8 and freestream Reynolds number of 12.2×10^6 m^{-1} ($Re_{R_N} = 63,440$), show that the spectra of wall-pressure and heat-transfer fluctuations recover the signature of the axisymmetric entropy-layer waves predicted by the nonmodal analysis. Nevertheless, the transition is anticipated to occur at a later stage, as indicated by the findings from the blunt cone experiments conducted by Jewell et al. [22] and Marineau et al. [23] in a Mach 6 facility at the Air Force Research Laboratory (AFRL) and during Mach 10 tests in the AEDC Hypervelocity Wind Tunnel Number, respectively. As summarized by Paredes et al. [6], there is a drop in the second Mack's mode N-factor at the transition onset location for $Re_{R_N} > 40,000$, but the transition onset continues to correlate with low values of the N-factor up to approximately $Re_{R_N} \approx 500,000$. The physical mechanisms responsible for the correlation of the transition onset location with low values of the Mack's mode N-factor are unknown. The potential interaction of the axisymmetric nonmodal entropy-layer disturbances with the Mack's second mode are investigated in the present work.

The popularity of solving the parabolized stability equations (PSE) stems from its economy as an efficient analysis tool to identify and propagate a single disturbance entity at specified frequency or a group of disturbances that are nearly phase synchronized with each other. Although the PSE have been used for linear and nonlinear stability analysis in weakly nonparallel flows, the limiting assumptions on the spatial gradients in the flow and the restriction of solution accuracy to the dominating mode hinders PSE application to flows with mode interactions [24]. The Nonlinear PSE (NPSE) presented by Bertolotti et al. [25] and Chang and Malik [26] are still affected by the limitations explained in Ref. [24] but in addition, the disturbance behavior of one frequency can affect the behavior of other frequencies through nonlinear interactions, allowing for the study of nonlinear evolution of linear disturbances as performed by Paredes et al. [27] on cones. Reference [27] not only reports an excellent agreement between the NPSE and DNS predictions, but also that nonlinear interactions of the primary linear nonmodal disturbances can lead to stationary streaks that amplify in the boundary layer and lead to transition onset for moderate amplitudes of the inflow disturbance. In this work, the linear nonmodal disturbances were used as the inflow for the nonlinear calculations. However, the nonlinear interactions can lead to different optimal results as shown by Ref. [28] for an incompressible Blasius boundary layer flow. In this work, we extend the linear nonmodal analysis performed in Refs. [6, 9] by including the nonlinear effects on disturbance development. By assuming a time periodic form for the perturbations, the harmonic Navier-Stokes equations (HNSE) are used as an efficient method to solve nonlinear disturbances. An inherent challenge in this development is related to the numerical treatment of time advancement. An explicit solver in time does not scale well when the spatial grid is refined and will eventually lead to convergence issues during the solution of the discretized HNSE. In contrast, solving implicitly in time allows for a significant performance gain resulting from the lack of restrictions on the time-stepping integration. However, the implicit formulation requires the inversion of a very large matrix and iterative methods can greatly reduce the computational requirements of a direct method [28]. Thus, the iterative methods form a significant component of efficient solutions to the HNSE.

The theoretical approach is outlined in Section II with a description of the governing equations as well as the implicit solution process. In Section III, the HNSE solver is verified against NPSE results for two separate cases: the nonlinear evolution of Tollmien-Schlichting waves in an incompressible flat-plate boundary layer flow and the development of Mack's second modes over a Mach 6 blunt cone. Linear and nonlinear nonmodal results are also presented for the Mach 6 blunt cone configuration. Concluding remarks are given in Section IV.

II. Theory

The harmonic linear Navier-Stokes equations (HLNSE) formulation of Refs. [6, 9] for the study of linear modal and nonmodal stability analysis of the boundary layer over blunt, circular cones at hypersonic conditions is extended to include nonlinear effects with the harmonic Navier-Stokes equations (HNSE) and study the nonlinear, nonmodal analysis of such configurations. The linear and nonlinear parabolized stability equations, LPSE and NPSE, respectively, are used to verify the HNSE solver.

A. Governing Equations for Modal and Nonmodal Disturbances

For the two-dimensional/axisymmetric geometries of interest here, the computational coordinates are defined as an orthogonal, body-fitted coordinate system, with (ξ, η, ζ) denoting the streamwise, wall-normal, and azimuthal coordinates, respectively, and (u, v, w) representing the corresponding velocity components. Density and temperature are denoted by ρ and T. The Cartesian coordinates are represented by (x, y, z). The vector of perturbation variables is denoted by $\tilde{\mathbf{q}}(\xi, \eta, \zeta, t) = (\tilde{\rho}, \tilde{u}, \tilde{v}, \tilde{w}, \tilde{T})^T$ and the vector of disturbance functions is $\breve{\mathbf{q}}(\xi, \eta, \zeta) = (\breve{\rho}, \breve{u}, \breve{v}, \breve{w}, \breve{T})^T$. The vector of basic state variables is $\bar{\mathbf{q}}(\xi, \eta, \zeta) = (\bar{\rho}, \bar{u}, \bar{v}, \bar{w}, \bar{T})^T$. For two-dimensional/axisymmetric geometries, the basic state variables are independent of the azimuthal coordinate.

For linear analysis, the perturbations can be assumed to be harmonic in time and in the azimuthal direction, which lead to the following expression for the perturbations,

$$\tilde{\mathbf{q}}(\xi, \eta, \zeta, t) = \breve{\mathbf{q}}(\xi, \eta) \exp\left[\mathrm{i}\left(m\zeta - \omega t\right)\right] + \text{c.c.}, \tag{1}$$

where m is the azimuthal wavenumber and ω is the angular frequency. In two-dimensional geometries, the azimuthal wavenumber m is substituted by the spanwise wavenumber β. The disturbance functions $\breve{\mathbf{q}}(\xi, \eta, \zeta)$ satisfy the HLNSE [6], which the linear operators depend on for the basic state variables and parameters, and on the angular frequency and azimuthal wavenumber of the perturbation.

For nonlinear analysis, the perturbation form of the HNSE is used. A fully implicit formulation is proposed by discretizing the azimuthal direction and the time domains with the periodic Fourier spectral collocation method [29, 30]. The definition of the first and second derivative matrix coefficients on a periodic grid depends on the choice of grid points, N, being even or odd. Here, N is always chosen odd for this discretization, and represents the number of Fourier modes being solved, n_ω, by $N = 2n_\omega + 1$. The computational domain is selected in the range $[0, 2\pi]$ and the computational mesh spacing is $h = 2\pi/N$. The elements of the first derivative operator, $\mathcal{D}$, are written as

$$\mathcal{D}_{i,j} = \begin{cases} 0, & i = j \\ \frac{1}{2}(-1)^{i+j} \csc\left[\frac{(i-j)\pi}{N}\right], & i \neq j \end{cases} \tag{2}$$

where $i, j = 1, ..., N$. The computational domain is scaled to the physical domain by using the selected fundamental wavelength for the azimuthal direction or fundamental frequency for time.

The HNSE, $\mathbf{F}(\tilde{\mathbf{q}}) = \mathbf{0}$, are solved with the Newton-Raphson method as

$$\mathbf{L}\Delta\tilde{\mathbf{q}} = -\mathbf{F}, \tag{3}$$

where $\Delta\tilde{\mathbf{q}}$ denotes the change in perturbation variables and $\mathbf{L}$ is the Jacobian of the nonlinear equations, $\mathbf{L} = \frac{\partial \mathbf{F}}{\partial \mathbf{q}}$ and, therefore, is equivalent to the HLNSE operator. Following each Newton-Raphson iteration, the solution is updated with the solution of Eq. 3, $\tilde{\mathbf{q}}_{j+1} = \tilde{\mathbf{q}}_j + \Delta\tilde{\mathbf{q}}$ until convergence is achieved. The right-preconditioned GMRES method [31] is used to converge the linear system. The preconditioning is based on a simplified matrix that corresponds to the overall Jacobian, but without the cross derivative terms. The LU decomposition of the preconditioner matrix is performed with the sparse direct solver MUMPS [32, 33] for the first linear system solution, and is recomputed in the course of the nonlinear iterative steps if the GMRES method fails to converge. Pseudotransient continuation is used to facilitate the convergence of the solution [34].

The PSE approximation to the HNSE is based on isolating the rapid phase variations in the streamwise direction by introducing a phase term. Furthermore, the disturbance variables are expanded in terms of their truncated Fourier components assuming they are periodic in time as follows

$$\tilde{\mathbf{q}}(\xi, \eta, \zeta, t) = \sum_{n=-n_\omega}^{n_\omega} \hat{\mathbf{q}}_n(\xi, \eta) \exp\left[\mathrm{i}\left(\int_{\xi_0}^{\xi} \alpha_n(\xi')\, \mathrm{d}\xi' + m\zeta - n\omega t\right)\right], \tag{4}$$

where α is the streamwise wavenumber and n_ω is the number of Fourier modes. The LPSEs neglect the nonlinear terms, while the NPSEs retain the nonlinear terms as a forcing term. Additional details of the PSE method and current implementation can be found in Refs. [25, 27, 35–39].

For the nonmodal analysis, a variational formulation based on the HNSE is used. The optimal initial disturbance, $\tilde{\mathbf{q}}_0$, is defined as the initial (i.e., inflow) condition at ξ_0 that maximizes the objective function, J, which can be defined as a measure of disturbance growth over a specified interval $[\xi_0, \xi_1]$ or other relevant quantities, such as those related to the skin friction or the heat transfer. The definition used in the present study correspond to the outlet energy gain [40, 41] that is defined as

$$G_E = \frac{E(\xi_1)}{E(\xi_0)}, \tag{5}$$

where E denotes the energy norm of $\tilde{\mathbf{q}}$. The energy norm is defined as

$$E(\xi) = \frac{1}{L_t L_\zeta} \int_t \int_\zeta \int_\eta \tilde{\mathbf{q}}(\xi, \eta, \zeta, t)^H \mathbf{M}_E \tilde{\mathbf{q}}(\xi, \eta, \zeta, t)\, h_\xi\, h_\zeta\, \mathrm{d}\eta \mathrm{d}\zeta \mathrm{d}t, \tag{6}$$

where $\mathbf{M}_E$ is the energy weight matrix and the superscript H denotes conjugate transpose. The disturbance amplitude is defined as $A = \sqrt{E}$, and the amplitude gain is $G_A = \sqrt{G_E}$.

The nonlinear nonmodal analysis follows the same procedure as the linear analysis. The variational formulation of the problem to determine the maximum of the objective functional J leads to an optimality system (see Ref. [42] for linear analysis and Refs. [28, 43] for nonlinear analysis), which is solved in an iterative manner, starting from a random solution at ξ_0 that must satisfy the boundary conditions. The HNSE, $F(\tilde{\mathbf{q}}) = 0$, are used to solve for $\tilde{\mathbf{q}}$, and the optimality condition is used to obtain the initial condition for the integration of the adjoint equations, $\mathbf{L}^\dagger \tilde{\mathbf{q}}^\dagger = \mathbf{R}(\tilde{\mathbf{q}})$, where $\mathbf{R}(\tilde{\mathbf{q}})$ is a function of the direct solution [28, 43]. The iterative procedure finishes when the value of J has converged up to a certain tolerance.

B. Discretization and Boundary Conditions

High-order finite-difference schemes [44, 45] of sixth order are used to discretize the stability equations on a nonuniform grid along the wall-normal direction. For the results presented here, the wall-normal direction is discretized with $N_\eta = 81$, with the nodes clustered toward the wall. The discretized PSE are integrated along the streamwise coordinate by using second-order backward differentiation. The HNSE are discretized with a sixth-order, central scheme along the streamwise direction, by using a total of $N_\xi = 1201 - 1601$ points. The number of Fourier collocation points in time are varied from $N_t = 5$ to $N_t = 15$ to obtain converged solutions for higher Fourier modes. The number of discretization points in both streamwise and wall-normal directions as well as in time is varied in selected cases to ensure the numerical convergence of the solution up to the leading modes of interest.

No-slip, isothermal boundary conditions are used at the wall, i.e., $\hat{u} = \hat{v} = \hat{w} = \hat{T} = 0$ or $\breve{u} = \breve{v} = \breve{w} = \breve{T} = 0$. The farfield boundary is set far enough to allow the decay of the perturbations for the incompressible case and just below the bow shock layer for the hypersonic case. The amplitude functions are forced to decay at the farfield boundary by imposing the Dirichlet conditions $\hat{\rho} = \hat{u} = \hat{w} = \hat{T} = 0$ or $\breve{\rho} = \breve{u} = \breve{w} = \breve{T} = 0$. For the HLNSE, the inflow condition is based on the solution of the PSE, and the perturbations are forced to decay at the outflow boundary with a sponge region.

III. Results

This section begins with the comparison of results based on the harmonic Navier-Stokes solver for a Blasius flow with the predictions obtained by using the nonlinear PSE solver from Paredes et al. [38]. After demonstrating a good agreement between the two sets of predictions, we consider an axisymmetric 7-degree half-angle cone with a nosetip radius of $R_N = 1.524$ mm at a freestream Mach number of 5.9 and freestream unit Reynolds number of 30.5×10^6 m^{-1}. Linear development of modal and nonmodal disturbances in this flow was studied by Paredes et al. [9]. The results presented in this section address both linear and nonlinear evolution of nonmodal disturbances. The freestream values of velocity, temperature, and density are used as the reference quantities for nondimensionalization.

A. Blasius Flow

To validate the HNSE solver, the nonlinear evolution of a planar Tollmien-Schlichting (TS) wave in a zero-pressure-gradient boundary-layer Blasius flow at $M_\infty = 0.001$ is studied. The fundamental wave is selected with a disturbance frequency of $\omega_1 = 0.0344$ s^{-1} and is initiated at $R_0 = 400$, where $R = \sqrt{Re_x}$. As previously explained, we use a fully

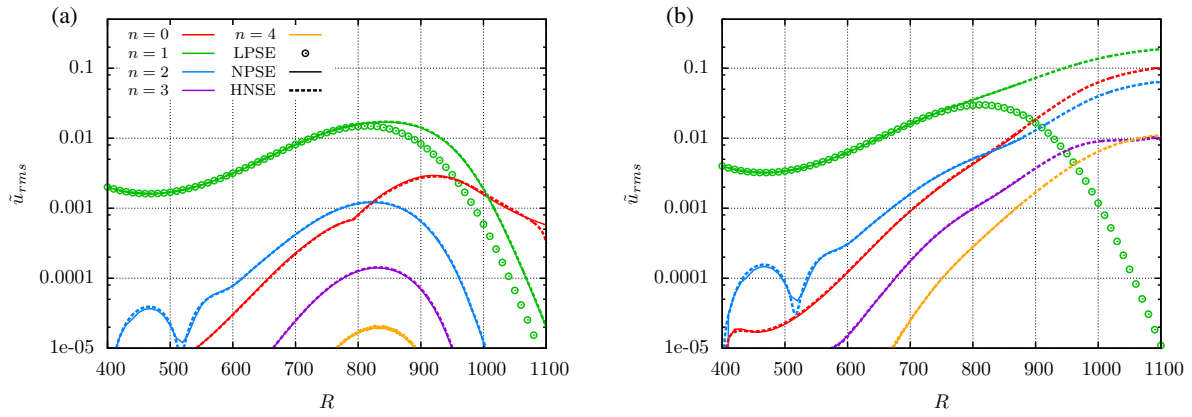

Fig. 1 Evolution of the root-mean-square amplitude of the streamwise velocity disturbance in the Blasius boundary layer, as computed with NPSE and HNSE for a fundamental planar disturbance with $\omega = 0.0344$ s^{-1} and an initial amplitude of (a) $\tilde{u}_{rms} = 0.002$ and (b) $\tilde{u}_{rms} = 0.004$. The linear evolution of the fundamental mode computed with LPSE is also included.

implicit formulation of the HNSE, where the time is discretized with Fourier collocation points with a domain equal to the period of the fundamental wave, $L_t = 2\pi/\omega_1$. The number of points N defines the number of Fourier modes being solved by $N = 2n_\omega + 1$, where n_ω includes the mean flow distortion, the fundamental frequency, and its harmonics. For the present verification of the solver, the first three harmonics are sought and $N_t = 2 \times (3 + 1) + 1 = 9$ collocation points are used. The spanwise direction is not discretized because only planar waves are considered.

Figures 1(a) and 1(b) display the streamwise evolution of the root-mean-square amplitudes of streamwise velocity perturbations computed with both NPSE and HNSE for two initial amplitudes of the fundamental wave, $\tilde{u}_{rms,0} = 0.002$ and $\tilde{u}_{rms,0} = 0.004$, respectively. Predictions pertaining to the linear evolution calculated with LPSE are also shown for comparison. For both initial amplitudes, the HNSE and NPSE predictions indicate very good agreement for the mean flow distortion ($n = 0$) as well as for the amplitudes of the fundamental mode ($n = 1$) and its harmonics ($n > 1$). For the lower initial amplitude ($\tilde{u}_{rms,0} = 0.002$), the fundamental mode follows the linear trend until $R \approx 750$, where the nonlinear effects become important and the fundamental wave is further destabilized. Even at the higher amplitude of $\tilde{u}_{rms,0} = 0.004$, good agreement between NPSE and HNSE is still observed up to $R \approx 875$, where the NPSE iterations fail to converge due to strong nonlinear effects. Therefore, this simple example highlights the potential utility of the HNSE for cases with higher initial disturbance amplitudes.

For this incompressible flow, increasing the initial disturbance amplitude leads to a continued growth in the fundamental disturbance amplitude, well past the upper branch location (slightly downstream of $R = 800$) as predicted by the LPSE in Fig. 2. The LPSE predict a peak amplitude growth of nearly 8 with respect to the initial station. For low initial amplitudes of up to $\tilde{u}_{rms,0} = 0.001$, the increase in fundamental mode amplitude predicted via the NPSE is very similar to the LPSE predictions. However, the effects of nonlinearity become quite prominent for $\tilde{u}_{rms,0} = 0.003$, where the peak disturbance amplification reaches almost $|\tilde{u}|/|\tilde{u}_0| = 20$ at $R = 1000$. For the largest initial amplification shown, the fundamental wave continues to amplify across the entire streamwise domain, leading to $|\tilde{u}|/|\tilde{u}_0| = 45$ at $R = 1100$. Therefore, nonlinear effects strongly destabilize the TS instabilities.

B. Mach 6 Flow over Blunt Circular Cones

Following the study of linear analyses of modal and nonmodal disturbance evolution on blunt cones by Paredes et al. [9], the nonlinear evolution of Mack's second mode (MM) disturbances is analyzed with NPSE and HNSE for the lower Reynolds number case of $Re_\infty = 30.5 \times 10^6$ m^{-1}, with a nosetip of 1.524 mm radius (case II in the aforementioned work).

The flow conditions and geometry are based upon the tests conducted by Jewell et al. [22] in the U.S. Air Force Research Laboratory (AFRL) Mach 6 high-Reynolds-number facility. The computational freestream conditions are given here in Table 1. The selection of this case is motivated by the low transition N-factor value of $N_{\mathrm{MM}}(\xi_T) = 3.75$ at the measured transition location, $\xi_T = 0.223$ m. For a sharper cone with $R_N = 0.508$ mm and $Re_\infty = 91.5 \times 10^6$ m^{-1}, the measured onset of transition corresponds to streamwise location with $N_{\mathrm{MM}}(\xi_T) = 7.77$. Therefore, the drop in

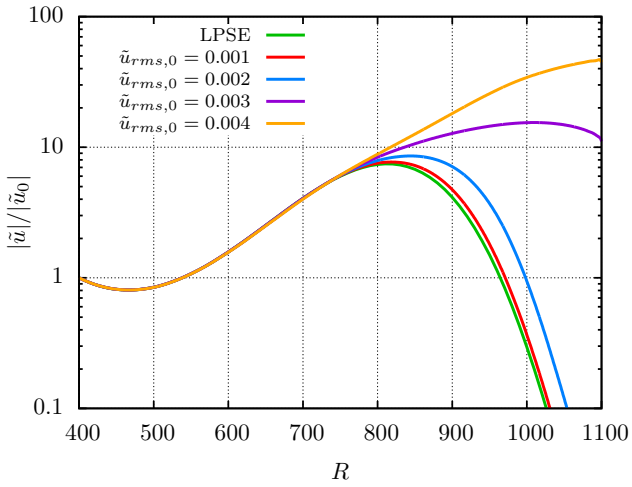

Fig. 2 Evolution of the normalized streamwise velocity amplitude of the fundamental disturbance with $\omega_1 = 0.0344$ s^{-1} in the Blasius boundary layer, as computed with HNSE with different initial amplitudes. The linear evolution of the fundamental mode computed with LPSE is also included.

Table 1 Details of the AFRL configuration used in the present study, including the measured transition location (ξ_T) from Ref. [22], the Mack-mode N-factor ($N_{\mathrm{MM}}(\xi_T)$) at the transition location, along with the frequency of the most amplified disturbance ($F_{\mathrm{MM}}(\xi_T)$). The flow conditions are $M_\infty = 5.9$, $\bar{T}_\infty = 76.74$ K, $\bar{T}_w = 300$ K, and $\bar{T}_w/\bar{T}_{w,ad} = 0.57$.

R_N [mm]	Re_∞ [$\times 10^6$ m^{-1}]	Re_{R_N} [$\times 10^3$]	ξ_T [m]	$N_{\mathrm{MM}}(\xi_T)$	$F_{\mathrm{MM}}(\xi_T)$ [kHz]
1.524	30.5	46.48	0.223	3.75	660

$N_{\mathrm{MM}}(\xi_T)$ is believed to be related to the effects of nose bluntness.

The verification of the HNSE solver for an axisymmetric configuration in high-speed flow is performed by comparing with NPSE results for the evolution of planar MM with a disturbance frequency of $f = 660$ kHz. The inflow location is selected at $\xi = 0.155$ m in order to lower computational cost and was verified to not significantly change the results as opposed to a location further upstream. The evolution of the root-mean-square of temperature disturbances computed with the NPSE and HNSE, as well as the linear evolution calculated with LPSE, are shown in Figures 3(a) and 3(b) for two different initial amplitudes of $\tilde{u}_{rms,0} = 0.001$ and $\tilde{u}_{rms,0} = 0.004$, respectively. The fundamental mode ($n = 1$) follows the linear trend until $\xi \approx 0.22$ and $\xi \approx 0.2$ m for $\tilde{u}_{rms,0} = 0.001$ and $\tilde{u}_{rms,0} = 0.004$, respectively. Downstream, the nonlinear effects become important and the fundamental wave is stabilized (in contrast to the Blasius configuration, where the fundamental wave was destabilized as seen in Fig. 2). The HNSE and NPSE results agree for all modes ($n = 0, 1, 2, 3, 4$). However, NPSE are not obtained downstream of $x = 0.215$ m for the larger initial amplitude due to the strong nonlinear effects. The dampening effect of the nonlinear interactions on the temperature disturbances is shown in Fig. 4. As the initial disturbance amplitude is increased, the normalized temperature maximum decreases. Therefore, the nonlinear effects lead to saturation of the MM disturbances as noted in previous work by Li et al. [46].

The linear nonmodal analysis of the boundary layer over the blunt cone geometry at the conditions of Table 1 was studied in Ref. [9] with the reduced form of the HLNSE (RHLNSE) that uses the Vigneron parameter to allow a parabolic integration of the HLNSE. However, the amplification of modal instabilities is not well captured by the RHLNSE. Here, the HLNSE are used to study the linear nonmodal amplification of planar disturbances ($m = 0$). The inflow optimization location is selected at $\xi_0 = 0.05$ m, although nearly equivalent results were obtained with inflow locations close to the nosetip. The final optimization location is selected to coincide with the measured transition location of $\xi_1 = \xi_T = 0.223$ m. Figure 5(a) shows the amplitude gain predicted by the linear analysis, i.e., $G_A = \sqrt{G_E}$, as a function of the disturbance frequency. The narrow bandwidth centered at $f = 660$ kHz corresponds to the MM wave. The disturbance frequency corresponding to the maximum N_{MM} at the transition location of $f_{MM} = 660$ kHz [9] coincides with the frequency for maximum optimal gain. The nonmodal entropy-layer disturbances are also amplified, albeit with lower amplification gains across the selected frequency range up to 800 kHz. Figure 5(b) shows the optimal

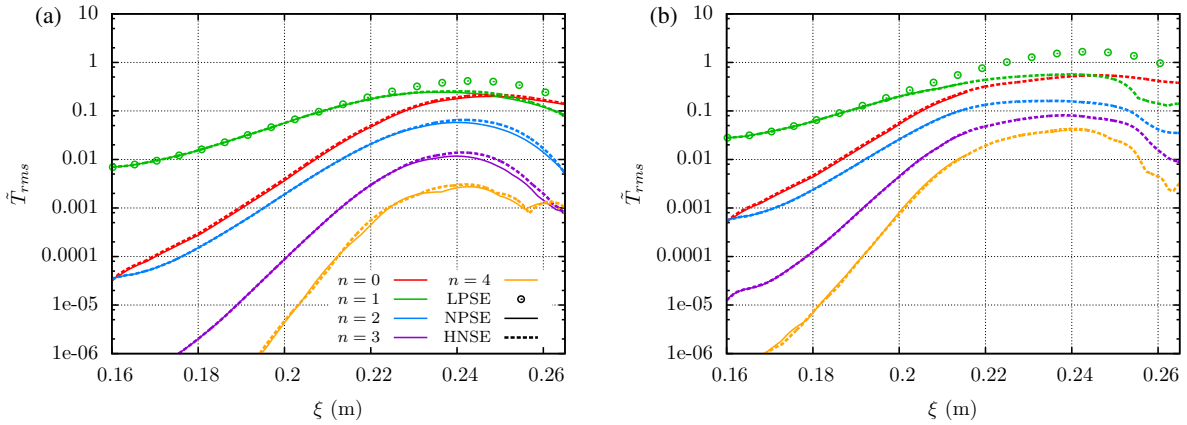

Fig. 3 Evolution of the root-mean-square amplitude of the temperature disturbance computed with NPSE and HNSE for a fundamental planar disturbance with f = 660 kHz and an initial amplitude of (a) $\tilde{u}_{rms}$ = 0.001 and (b) $\tilde{u}_{rms}$ = 0.004 for the Mach 6 flow over a blunt circular cone. The linear evolution of the fundamental mode computed with LPSE is also included.

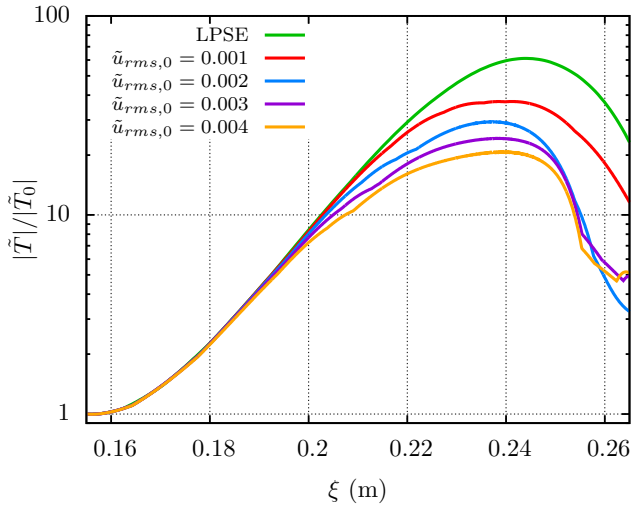

Fig. 4 Evolution of the normalized temperature amplitude of the fundamental disturbance with f_1 = 660 kHz for the Mach 6 flow over a blunt, circular cone as computed with HNSE with different initial amplitudes. The linear evolution of the fundamental mode computed with LPSE is also included.

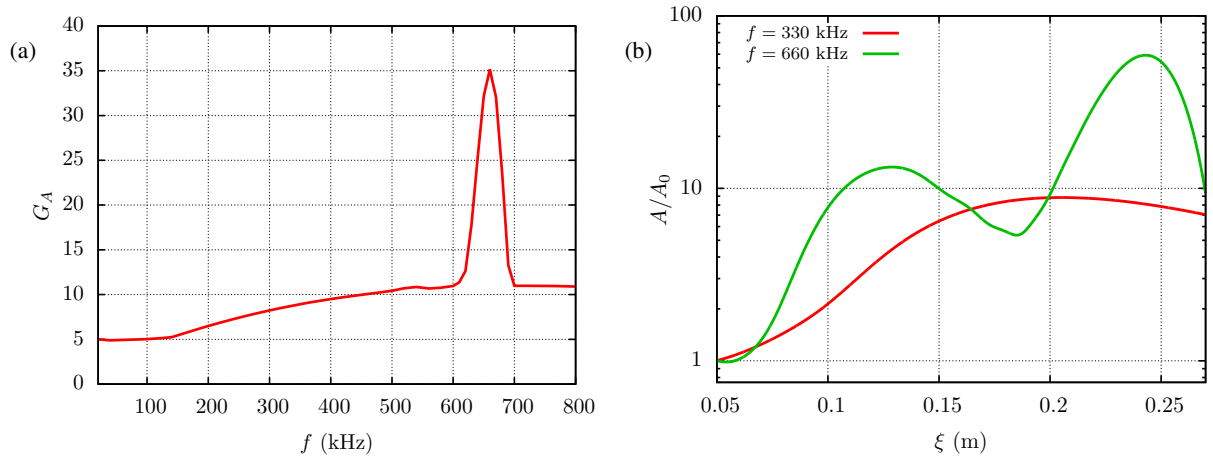

Fig. 5 Spectrum of (a) amplitude gain as a function of frequency for planar waves ($m = 0$) and (b) streamwise evolution of amplitude for $f = 330$ and 660 kHz with respect to streamwise location.

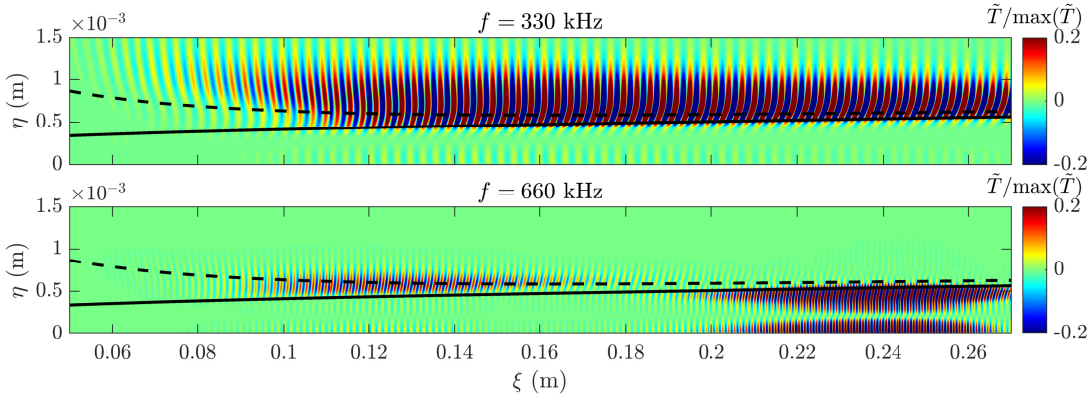

Fig. 6 Contours of the normalized temperature for the linear, optimal disturbances with $f = 330$ and 660 kHz and an optimization interval of $(\xi_0, \xi_1) = (0.05, 0.223)$ m. The solid and dashed black lines indicate the edge of the boundary layer, δ_h, and the edge of the entropy layer, δ_S, respectively.

disturbance amplitude evolution for $f = 330$ and 660 kHz. The evolution of the optimal disturbances are clearly different between the two frequencies. Whereas the lower frequency monotonically gets amplified nearly up to the maximum amplitude location somewhat upstream of the optimization station ($\xi = 0.223$ m), the higher frequency disturbance has a first peak near $\xi = 0.13$ m and then decays and begins to amplify again to reach its overall maximum near $\xi = 0.24$ m. The contours of normalized temperature fluctuation $\tilde{T}/\max(\tilde{T})$ for both frequencies ($f = 330$ and 660 kHz) are shown in Figures 6(a) and 6(b), respectively. The lower frequency and the first peak of the higher frequency disturbances correspond to the nonmodal entropy-layer disturbances with peaks along the edge of the entropy layer (i.e., outside of the boundary layer). As the disturbance amplitude decreases downstream of the first peak for the $f = 660$ kHZ disturbance, the second mode becomes dominant, with the peak of temperature fluctuations occurring inside the boundary layer.

The nonlinear nonmodal analysis is used to investigate the potential interactions between the nonmodal entropy-layer disturbances with $f = 330$ kHz and MM waves with $f = 660$ kHz. The inflow forcing is limited to the fundamental wave to avoid the introduction of the high frequency disturbance at the inflow. The dependency of the amplitude gain on the initial amplitude $A_0 = \sqrt{E_0}$ is shown in Fig. 7(a). The two separate curves in this figure represent the fact that the optimization process converged to two different values of the amplitude gain over an intermediate range of initial amplitudes, depending on the initial guess. The linear optimal disturbance was selected as initial guess for the lowest initial amplitude, and the final solution at a given amplitude was successively used as initial guess for the next higher amplitude. However, the resulting gain was found to change drastically for sufficiently large initial amplitudes as

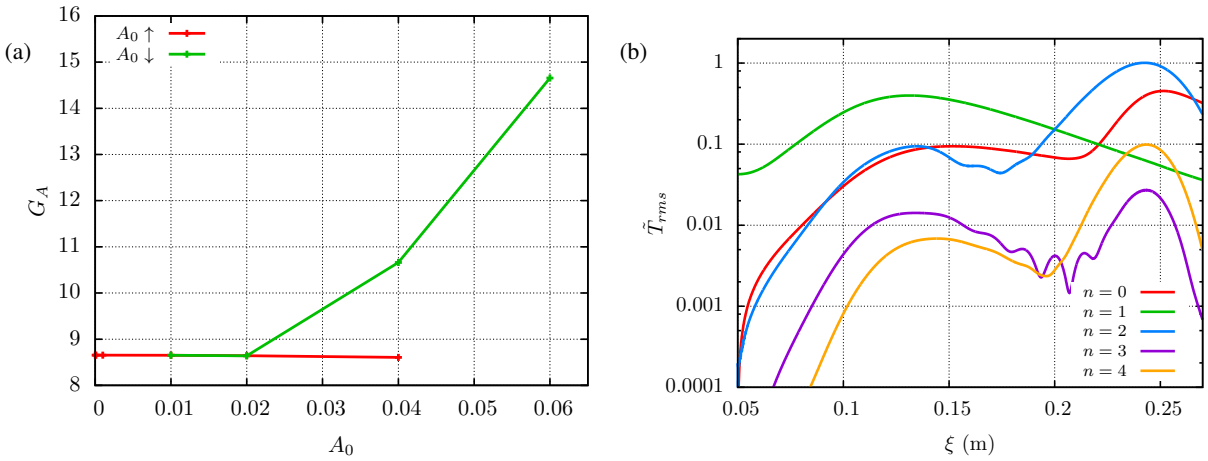

Fig. 7 Evolution of the (a) amplitude gain as a function of initial disturbance amplitude with a fundamental frequency of $f_1 = 330$ kHz and (b) evolution of the root-mean-square amplitude of the optimal temperature disturbance for the $n = 0$ mean flow distortion, $n = 1$ fundamental wave, and its harmonics $n = 2, 3, 4$ with an initial amplification of $A_0 = 0.06$. In the legend of subfigure (a), $A_0 \uparrow$ and $A_0 \downarrow$ refer to a lower and higher amplitude used as initial guess respectively.

indicated by the green curve in Fig. 7(a). The evolution of the leading Fourier harmonics from the nonlinear optimal disturbance corresponding to $A_0 = 0.06$ is plotted in Fig. 7(b). This disturbance has an energy gain of nearly 15 as seen from Fig. 7(a). The MM wave with $f = 660$ kHz (first harmonic of the inflow disturbance frequency) is generated by the nonlinear self-interaction of the initially seeded $f = 330$ kHz disturbance as it undergoes a nonmodal growth. The highest amplitude is observed somewhat downstream of the optimization location at $\xi \approx 0.24$ m, and it surpasses the peak of the fundamental wave which occurs around $\xi = 0.125$ m. Therefore, the entropy-layer disturbances excited near the nosetip can excite the high frequency MM disturbances somewhat upstream of their lower branch neutral station for the MM modes and the subsequent amplification of these MM disturbances can lead to an overall increase in the disturbance energy beyond the linear evolution of the same entropy-layer disturbances.

The temperature contours of the mean flow distortion ($f_0 = 0$ kHz), the fundamental mode ($f_1 = 330$ kHz), and its first harmonic ($f_2 = 660$ kHz) are shown in Fig. 8 for an initial amplitude of $A_0 = 0.06$. The initial phase of mean flow distortion includes a temperature disturbance in the vicinity of the entropy layer edge, contributing to a higher temperature above the edge and lower temperature below the edge. Downstream of $\xi = 0.12$ m, the negative correction to basic state temperature penetrates the boundary layer edge, progressively spreading to the interior portions of the boundary layer. Downstream of $\xi = 0.223$ m, the negative temperature correction has spread through the majority of the boundary layer and is accompanied by a thin layer of positive temperature correction between the boundary layer edge and the entropy layer edge. The temperature contours associated with the fundamental wave are similar to the linear nonmodal results in Fig. 6 with the exception that the fluctuations peak around $\xi = 0.13$ m and do not extend as far in the wall-normal direction. Consistent with the aforemention discussion, the evolution of the temperature disturbances at the first harmonic ($f_2 = 660$ kHz) is similar to the results of the linearly optimal disturbance with $f = 660$ kHz shown in Fig. 6. Thus, two regions of disturbance growth are observed, the first corresponding to the entropy layer disturbances, and the second one to the MM instability.

IV. Summary and Concluding Remarks

A fully implicit formulation of the harmonic Navier-Stokes equations (HNSE) is presented for the nonlinear nonmodal analysis of disturbances in the Mach 6 flow over blunt, circular cone. Previous studies [6, 9] performed linear, nonmodal analysis of the same flow and found the amplification of planar and oblique traveling disturbances that peak within the entropy layer for moderate to large nosetip bluntness values. The extension of the linear nonmodal analysis based on the harmonic linearized Navier-Stokes equations (HLNSE) to include nonlinear interactions enables us to investigate the coupling among a broader set of disturbances, including potential interactions involving nonmodal entropy layer waves and Mack's second mode disturbances.

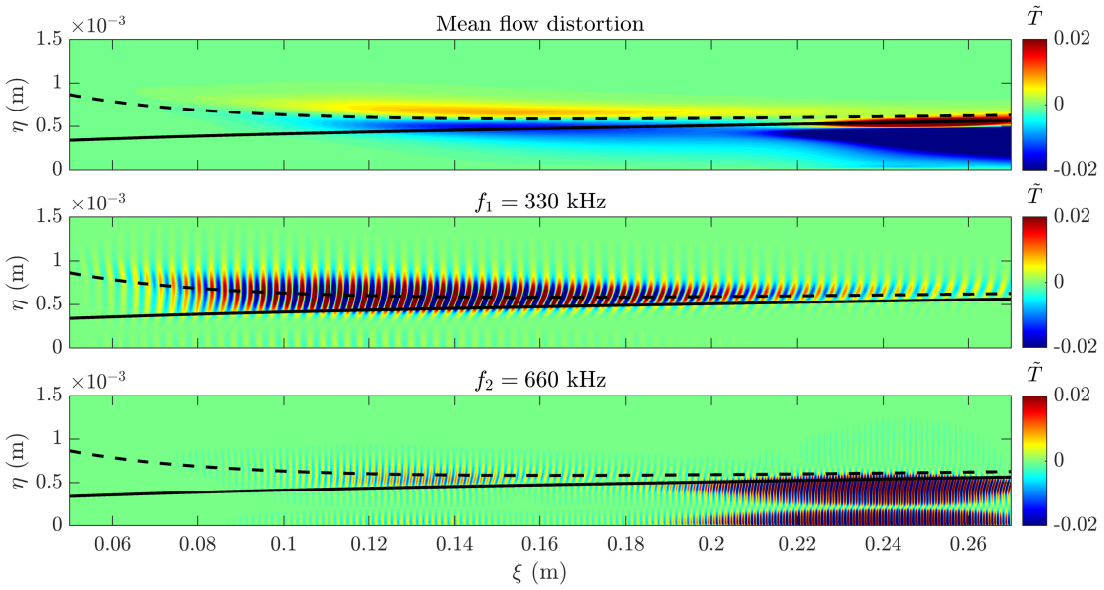

Fig. 8 Contours of temperature for the mean flow distortion, fundamental frequency ($f = 330$ kHz), and the first harmonic ($f = 660$ kHz) of the optimal disturbance computed by using the HNSE and $(\xi_0, \xi_1) = (0.05, 0.223)$ m. The solid and dashed black lines indicate the edge of the boundary layer, δ_h, and the edge of the entropy layer, δ_S, respectively.

The predictions of the HNSE solver are compared with NPSE results for the nonlinear evolution of modal instabilities in a low-speed Blasius boundary layer flow and a Mach 6 flow over a blunt circular cone. The predicted evolution of both a planar Tollmien-Schlichting wave in the Blasius flow and a planar Mack's second mode in the hypersonic flow over the cone showed excellent agreement with the NPSE results. Furthermore, for both flow configurations, the HNSE led to converged predictions for relatively high initial amplitudes where the NPSE failed to converge due to strong nonlinear effects. The nonlinear analysis for the blunt cone case was extended to include the nonmodal evolution of an inflow disturbance generated near the nose tip with half the frequency of the most amplified Mack's second mode at the measured transition location. The results show how the nonmodal entropy-layer disturbance can trigger excitation of Mack's second mode waves that undergo significant amplification downstream, to yield a continued growth in the overall disturbance energy. The additional receptivity mechanism associated with this path could contribute to higher initial amplitudes of the Mack's second mode disturbances, and hence, to a reduction in the transition N-factor in this flow.

The present work focuses on the linear and nonlinear development of planar waves. However, the nonlinear nonmodal analysis with the addition of three-dimensional disturbances would allow identification of the most dangerous inflow disturbances that would lead to the earliest onset of transition, especially in cases where the modal amplification alone is insufficient to cause transition. The addition of the third dimension represents a challenge for the solution of the linearized system. Therefore, iterative techniques based on suitable preconditioning are being further investigated to overcome those difficulties and allow for the fully implicit solution of the HNSE for a nonlinear, nonmodal analysis for three-dimensional disturbances.

Acknowledgments

This material is based upon research supported in part by the U. S. Office of Naval Research under award number N00014-20-1-2261, in part by the Hypersonic Technology Project (HTP) under the NASA Aeronautics Research Mission Directorate (ARMD). The development of the iterative solver is supported by the NASA Langley Research Center under the CIF/IRAD Program. Computational resources supporting this work were provided by the DoD High Performance Computing Modernization Program and the NASA K Cluster at Langley Research Center.

References

[1] Fedorov, A. V., "Transition and Stability of High-Speed Boundary Layers," *Annu. Rev. Fluid Mech.*, Vol. 43, 2011, pp. 79 –95.

[2] Zhong, X., and Wang, X., "Direct Numerical Simulation on the Receptivity, Instability, and Transition of Hypersonic Boundary Layers," *Annunal Review of Fluid Mechanics*, Vol. 44, 2012, pp. 527–561. doi:10.1146/annurev-fluid-120710-101208.

[3] Schneider, S., "Developing Mechanism-Based Methods for Estimating Hypersonic Boundary-Layer Transition in Flight: The Role of Quiet Tunnels," *Progress in Aerospace Sciences*, Vol. 72, 2015, pp. 17–29. doi:10.1016/j.paerosci.2014.09.008.

[4] Schneider, S., "Hypersonic Laminar-Turbulent Transition on Circular Cones and Scramjet Forebodies," *Progress in Aerospace Sciences*, Vol. 40, 2004, pp. 1–50. doi:10.1016/j.paerosci.2003.11.001.

[5] Stetson, K., "Nosetip Bluntness Effects on Cone Frustum Boundary Layer Transition in Hypersonic Flow," AIAA Paper 83-1763, 1983. doi:10.2514/6.1983-1763.

[6] Paredes, P., Choudhari, M., Li, F., Jewell, J., Kimmel, R., Marineau, E., and Grossir, G., "Nosetip Bluntness Effects on Transition at Hypersonic Speeds: Experimental and Numerical Analysis," *Journal of Spacecraft Rockets*, Vol. 56, No. 2, 2019. doi:10.2514/1.A34277.

[7] Lysenko, V., "Influence of the Entropy Layer on the Stability of a Supersonic Shock Layer and Transition of the Laminar Boundary Layer to Turbulence," *Applied Mechanics and Technical Physics*, Vol. 31(06), 1990, p. 868 (5 pages).

[8] Goparaju, H., Unnikrishnan, S., and Gaitonde, D., "Effects of Nose Blutness on Hypersonic Boundary-Layer Receptivity and Stability," *Journal of Spacecraft Rockets*, Vol. 58, No. 3, 2021. doi:10.2514/I.A34829.

[9] Paredes, P., Choudhari, M., Li, F., Jewell, J., and Kimmel, R., "Nonmodal Growth of Traveling Waves on Blunt Cones at Hypersonic Speeds," *AIAA Journal*, Vol. 57, No. 11, 2019. doi:10.2514/1.J058290.

[10] Scholten, A., Goparaju, H., Gaitonde, D., Paredes, P., Choudhari, M., and Li, F., "Linear Disturbance Amplification Over Blunted Flat Plates in High-Speed Flows," AIAA Paper 2022-3471, 2022. doi:10.2514/6.2022-3471.

[11] Hill, J., "Experimental Measurements of Hypersonic Instabilities over Ogive-Cylinders at Mach 6," Master's thesis, Air Force Institute of Technology, 2020.

[12] Hill, J., Oddo, R., Komives, J., Reeder, M., Borg, M., and Jewell, J., "Experimental Measurements of Hypersonic Instabilities over Ogive-Cylinder at Mach 6," AIAA Paper 2021-0153, 2021. doi:10.2514/6.2021-0153.

[13] Reshotko, E., "Boundary Layer Transition, Instability and Control," AIAA Paper 94-0001, 1994. doi:10.2514/6.1994-0001.

[14] Greenwood, R., "Measurements of Entropy-Layer Instabilities over Cone-Ogive-Cylinders at Mach 6," Ph.D. thesis, Purdue University, 2014.

[15] Scholten, A., Paredes, P., Hill, J., Borg, M., Jewell, J., and Choudhari, M., "Linear Instabilities over Ogive-Cylinder Models at Mach 6," *AIAA Journal*, Vol. 60, No. 8, 2022. doi:10.2514/1.J061611.

[16] Hartman, A., Hader, C., and Fasel, H., "Nonlinear Transition Mechanism on a Blunt Cone at Mach 6: Oblique Breakdown," *Journal of Fluid Mechanics*, Vol. 915, 2021, p. R2. doi:10.1017/jfm.2021.109.

[17] Duan, L., Choudhari, M., Chou, A., Munoz, F., Radespiel, R., Schilden, T., Schrörder, W., Marineau, E., Casper, K., Chaudhry, R., Candler, G., Gray, K., and Schneider, S., "Characterization of Freestream Disturbances in Conventional Hypersonic Wind Tunnels," *Journal of Spacecraft Rockets*, Vol. 56, No. 2, 2019, pp. 357–368. doi:10.2514/1.A34290.

[18] Duan, L., Nicholson, G., Huang, J., Casper, K., Wagnild, R., and Bitter, N., "Direct Numerical Simulations of Nozzle-Wall Pressure Fluctuations in a Mach 8 Wind Tunnel," AIAA Paper 2019-0874, 2019. doi:10.2514/6.2019-0874.

[19] Hildebrand, N., Choudhari, M. M., Deegan, C. P., Huang, J., and Duan, L., "Direct Numerical Simulation of Acoustic Disturbances in a Hypersonic Two-Dimensional Nozzle Configuration," *AIAA Journal*, Vol. 60, No. 6, 2022, pp. 3452–3463.

[20] Hildebrand, N. J., Choudhari, M. M., and Duan, L., "Effect of the Reynolds Number on the Freestream Disturbance Environment in a Mach 6 Nozzle," AIAA Paper 2022-3776, 2022.

[21] Liu, Y., Schuabb, M., Duan, L., Paredes, P., and Choudhari, M., "Interaction of a Tunnel-Like Acoustic Disturbance Field With a Blunt Cone Boundary Layer at Mach 8," AIAA Paper 2022-3250, 2022. doi:10.2514/6.2022-3250.

[22] Jewell, J., Kennedy, R., Laurence, S., and Kimmel, R., "Transition on a Variable Bluntness 7-Degree Cone at High Reynolds Number," AIAA Paper 2018-1822, 2018. doi:10.2514/6.2018-1822.

[23] Marineau, E., Moraru, C., Lewis, D., Norris, J., Lafferty, J., Wagnild, R., and Smith, J., "Mach 10 Boundary-Layer Transition Experiments on Sharp and Blunted Cones," AIAA Paper 2014-3108, 2014. doi:10.2514/6.2014-3108.

[24] Towne, A., Rigas, G., and Colonius, T., "A Critical Assessment of the Parabolized Stability Equations," *Theoretical and Computational Fluid Dynamics*, Vol. 33, 2019, pp. 359–382. doi:10.1007/s00162-019-00498-8.

[25] Bertolotti, F., Herbert, T., and Spalart, P., "Linear and Nonlinear Stability of the Blasius Boundary Layer," *Journal of Fluid Mechanics*, Vol. 242, 1992, pp. 441–474.

[26] Chang, C.-L., and Malik, M., "Oblique-Mode Breakdown and Secondary Instability in Supersonic Boundary Layers," *Journal of Fluid Mechanics*, Vol. 273, 1994, pp. 323–360. doi:10.1017/S0022112094001965.

[27] Paredes, P., Choudhari, M., and Li, F., "Mechanism for Frustum Tranistion over Blunt Cones at Hypersonic Speeds," *Journal of Fluid Mechanics*, Vol. 894, 2020, p. A22. doi:10.1017/jfm.2020.261.

[28] Rigas, G., Sipp, D., and Colonius, T., "Nonlinear Input/output Analysis: Application to Boundary Layer Transition," *Journal of Fluid Mechanics*, Vol. 911, 2021, p. A15. doi:10.1017/jfm.2020.982.

[29] Boyd, J., *Chebyshev and Fourier spectral methods*, Springer, 1989.

[30] Canuto, C., Hussaini, M., Quarteroni, A., and Zang, T., *Spectral methods in fluid dynamics*, Springer, 1987.

[31] Saad, Y., *Iterative methods for sparse linear systems*, PWS Publishing, 1996.

[32] Amestoy, P., Duff, I., Koster, J., and L'Excellent, "A Fully Asynchronous Multifrontal Solver using Distributed Dynamic Scheduling," *SIAM Journal of Matrix Analysis and Applications.*, Vol. 1, 2001, pp. 15–41.

[33] Amestoy, P., Guermouche, A., L'Excellent, J.-Y., and Pralet, S., "Hybrid Scheduling for the Parallel Solution of Linear Systems," *Parallel Computing*, Vol. 2, 2006, pp. 136–156.

[34] Kelley, C. T., and Keyes, D. E., "Convergence Analysis of Pseudo-Transient Continuation," *SIAM Journal on Numerical Analysis*, Vol. 35, No. 2, 1996, pp. 508–523. doi:10.1137/S0036142996304796.

[35] Bertolotti, F., and Herbert, T., "Analysis of the Linear Stability of Compressible Boundary Layers using PSE," *Theoretical and Computational Fluid Dynamics*, Vol. 3, 1991, pp. 117–124.

[36] Chang, C., Malik, M., Erlebacher, G., and Hussaini, M., "Compressible Stability of Growing Boundary Layers using Parabolized Stability Equations," AIAA Paper 1991-1636, 1991. doi:10.2514/6.1991-1636.

[37] Herbert, T., "Parabolized Stability Equations," *Annunal Review of Fluid Mechanics*, Vol. 29, 1997, pp. 245–283.

[38] Paredes, P., Hanifi, A., Theofilis, V., and Henningson, D., "The Nonlinear PSE-3D Concept for Transition Prediction in Flows With a Single Slowly-Varying Spatial Direction," *Procedia IUTAM*, Vol. 14C, 2015, pp. 35–44.

[39] Paredes, P., Choudhari, M., and Li, F., "Instaiblity Wave-Streak Interactions in a Supersonic Boundary Layer," *Journal of Fluid Mechanics*, Vol. 831, 2017, pp. 524–553. doi:10.1017/jfm.2017.630.

[40] Andersson, P., Berggren, M., and Henningson, D., "Optimal Disturbances and Bypass Transition in Boundary Layers," *Physics of Fluids*, Vol. 11, 1999, pp. 134–150. doi:10.1063/1.869908.

[41] Luchini, P., "Reynolds-Number-Independent Instability of the Boundary Layer over a Flat Surface: Optimal Perturbations," *J. Fluid Mech.*, Vol. 404, 2000, pp. 289–309. doi:10.1017/S0022112099007259.

[42] Paredes, P., Choudhari, M., Li, F., and Chang, C.-L., "Optimal Growth in Hypersonic Boundary Layers," *AIAA Journal*, Vol. 54, No. 10, 2016, pp. 3050–3061. doi:10.2514/1.J054912.

[43] Zuccher, S., Tumin, A., and Reshotko, E., "Parabolic Approach to Optimal Perturbations in Compressible Boundary Layers," *Journal of Fluid Mechanics*, Vol. 556, 2006, pp. 189–216. doi:10.1017/S0022112006009451.

[44] Hermanns, M., and Hernández, J., "Stable High-Order Finite-Difference Methods Based on Non-Uniform Grid Point Distributions," *International Journal for Numerical Methods in Fluids*, Vol. 56, 2008, pp. 233–255. doi:10.1002/fld.1510.

[45] Paredes, P., Hermanns, M., Le Clainche, S., and Theofilis, V., "Order 10^4 Speedup in Global Linear Instability Analysis using Matrix Formation," *Computer Methods in Applied Mechanics and Engineering*, Vol. 253, 2013, pp. 287–304. doi: 10.1016/j.cma.2012.09.014.

[46] Li, F., Choudhari, M., Chang, C.-L., and White, J., "Secondary Instability of Second Mode Disturbances in Hypersonic Boundary Layers," Tech. rep., NASA, 2012.